Journal of Materials Chemistry A

Light-Induced Degradation of Mixed-cation, Mixed-halide Perovskite: Observed Rates and Influence of Oxygen

Journal:	*Journal of Materials Chemistry A*
Manuscript ID	TA-ART-11-2024-007807.R1
Article Type:	Paper
Date Submitted by the Author:	18-Dec-2024
Complete List of Authors:	Cira, Spencer; University of Washington Department of Chemical Engineering Dunlap-Shohl, Wiley; University of Washington Department of Chemical Engineering Meng, Yuhuan; University of Washington Department of Chemical Engineering Sunkari, Preetham; University of Washington Department of Chemical Engineering Folch, Jordi; University of Washington Department of Chemical Engineering Hillhouse, Hugh; University of Washington Department of Chemical Engineering

SCHOLARONE™
Manuscripts

Light-Induced Degradation of Mixed-cation, Mixed-halide Perovskite: Observed Rates and Influence of Oxygen

Spencer G. Cira, Wiley A. Dunlap-Shohl, Yuhuan Meng, Preetham P. Sunkari, Jordi H. Folch, and Hugh W. Hillhouse*

Department of Chemical Engineering, Clean Energy Institute, and Molecular Engineering and

Sciences Institute, University of Washington, Seattle, WA 98195, U.S.A.

* Corresponding Author: h2@uw.edu

Abstract

Formamidinium-rich lead halide perovskite semiconductors comprise the absorber layer in the most efficient single-junction perovskite solar cells (PSCs) but suffer from chemical instability when exposed to high temperatures, moisture, oxygen, and light. Light-induced degradation (LID) is unavoidable in PSCs and can be slowed only by limiting the escape of decomposition products. Here, we study the LID of $FA_{0.8}Cs_{0.2}Pb(I_{0.83}Br_{0.17})_3$ thin films using *in-situ* and *ex-situ* optical spectroscopy, microscopy, and x-ray diffraction. The results reveal that the primary decomposition products under LID conditions are reduced lead-containing species that have broadband optical absorption. XPS reveals the presence of Pb^0, but it may coexist with partially reduced lead-containing species. We use *in-situ* sub-bandgap optical absorbance measurements to selectively

1   probe and quantitatively measure the formation rate of reduced lead species. We derive a rate law

2   for reduced-Pb formation (r_{Pb^0} estimated at ~3x10^{-10} mol/(m^{2}s) at 25 °C in N$_2$ under 1 sun photon

3   flux that would result in complete conversion of a 300 nm film in ~78 days), determine an

4   activation energy (~0.61 eV), determine an effective reaction order with respect to the flux of

5   above bandgap photons ($r_{Pb^0} \propto I_{in}^{0.72}$), and find that the wavelength of above bandgap photons

6   minimally affects the rate, suggesting that PbI$_2$ photolysis is not the mechanism for the formation

7   of decomposition products. These observations represent the first quantitative measurements of

8   the rate of formation of reduced lead species in perovskites and emphasize a unique interplay

9   among environmental stressors and degradation pathways for commercially relevant perovskite

10   materials.

11
12
13
14
15
16
17
18
19
20
21
22

23

24

25

26

27

1   Hybrid organic-inorganic perovskites with the chemical formula ABX_3 are a unique class of

2   semiconductors that exhibit simultaneous ease of fabrication (solution and/or vapor processing[1])

3   and excellent optoelectronic quality (long diffusion lengths and carrier lifetimes,[2] high absorption

4   coefficients,[3] and tunable bandgap[4]). Perovskite single-junction and perovskite-on-silicon tandem

5   photovoltaic (PV) cells have achieved 26.7% and 34.6%   power conversion efficiency[5],

6   respectively, as of December 2024. Despite their high defect concentration ($\sim 10^{15}$-10^{16} cm^{-3})

7   compared to conventional covalent semiconductors such as c-Si or GaAs ($<10^{12}$ cm^{-3}),[6–8] the ionic

8   nature of halide perovskites causes most of the defect energy levels to lie near the band edges or

9   within the bands, giving these materials their notable defect tolerance.[9] However, halide

10   perovskites are notoriously unstable in the presence of excess heat, above-bandgap photons,

11   oxygen, and moisture. In contrast to current commercial PV materials, halide perovskites readily

12   undergo chemical decomposition reactions when exposed to these stressors that can degrade

13   optoelectronic performance and have, up to this point, limited the lifetime of PSCs well below the

14   multidecade timescale necessary for commercial viability.[10] Stability of the absorber is thus a

15   primary factor hindering PSCs from realizing their commercial potential.

16   Mixed-cation, mixed-halide perovskites in which the A-site comprises mixtures of

17   formamidinium (FA), methylammonium (MA), and/or cesium, and the X-site comprises mixtures

18   of iodide and bromide, form the absorber layer in some of the most efficient lead-based PSCs and

19   display significant improvements in thermal stability and performance compared with the

20   archetypal perovskite $MAPbI_3$.[11–14] These compositions nevertheless exhibit low chemical

21   stability relative to conventional inorganic semiconductors.[15] While strong encapsulation may

22   prevent the ingress of oxygen and moisture for some time during the deployment of a PSC

23   module,[16] illumination is necessary for electrical energy production. Thus, studies of perovskite

1   degradation in inert environments under illumination are vital to probe what may represent the

2   ultimate performance-limiting case.

3   Previously, we reported the degradation kinetics of MAPbI$_3$[17] and the low bandgap lead-tin

4   perovskite composition FA$_{0.75}$Cs$_{0.25}$Pb$_{0.5}$Sn$_{0.5}$I$_3$[18] in response to oxygen, moisture, and

5   illumination. While measurable LID was not observed in these previous compositions, initial

6   investigations into the degradation of FA$_{0.8}$Cs$_{0.2}$Pb(I$_{0.83}$Br$_{0.17}$)$_3$ (referred to as FACsPbIBr)

7   revealed that unencapsulated films placed in an inert environment undergo decomposition when

8   exposed to illumination alone. In this study, we investigate this decomposition pathway with the

9   aims of identifying decomposition products and quantifying the rate of perovskite loss as a

10 function of environmental stressors, since quantitative kinetic measurements of light-induced

11 degradation do not currently exist in the literature.

12 The FACsPbIBr films used throughout this study were fabricated by an antisolvent wash method

13 (described in SI section 1). The pristine films are of high optoelectronic quality. Characterization

14 by x-ray diffraction (XRD), scanning electron microscopy (SEM), UV-Vis-NIR spectroscopy

15 (UV-vis), and photoluminescence (PL) spectroscopy are shown in Figure S1. The films have an

16 optical bandgap of ~1.66 eV and display steady-state quasi-Fermi level splitting of 1.29 eV under

17 1 sun equivalent illumination, which is >90% of the radiative limit (1.38 eV). Single-junction solar

18 cells made from the films with a p-i-n architecture (ITO/Poly-TPD/perovskite/C$_{60}$/BCP/Ag) have

19 efficiencies of ~17% (Fig. S2).

20 *Effects of LID on Mixed-cation, Mixed-halide Thin Films*. To identify the hallmarks of this

21 decomposition pathway, we performed *ex-situ* characterization of the FACsPbIBr films over a

22 period of LID. SI section 2 (Fig. S3b) includes the spectra of all illumination sources with a

23 description of calibration procedures. Sources are calibrated such that the incident above bandgap

1   absorbed photon flux is identical to that of the AM1.5 G solar spectrum (1.5×10^{21} photons/m^2/s

2   for a 1.66 eV absorber).

3   Unencapsulated FACsPbIBr films deposited on glass substrates were placed in a chemically

4   inert environment (dry N_2 glovebox) on a hotplate (shown schematically in Fig. S3a) set to 65°C

5   under 1 sun equivalent photon flux from a broad-spectrum 'white' LED (emission from 400-700

6   nm) and were periodically removed for characterization. Figure 1 shows the changes of the internal

7   absorbance spectrum (see SI section 4 for further analysis), absolute intensity photoluminescence

8   spectrum (AIPL), XRD pattern, and morphology over the course of degradation and demonstrates

9   that optical absorption is a leading indicator of this decomposition mode. The mean PL peak (Fig.

10   1b) redshifts modestly (~20 meV). The intensity drops rapidly, and a low energy shoulder develops

11   as degradation proceeds. Since the Br content is relatively low, we do not expect this low energy

12   shoulder to be a result of halide segregation but rather of shallow defect states.[19] The XRD patterns

13   (Fig. 1c) show that, over long periods of degradation, crystalline domains of metallic lead (Pb^0)

14   begin to form, which first become discernable at the 13-hour timepoint. Aside from small peaks

15   associated with PbI_2 (001-plane reflection at ~12.6°) and α-FAPbBr$_3$ (001-plane reflection at

16   ~14.8°) at very late stages of degradation, no other solid degradation products are observed in the

17   XRD patterns (zoomed-in plots and reference patterns are presented in SI section 3 and Fig. S4).

18   We also confirmed the presence of Pb^0 in degraded films with x-ray photoelectron spectroscopy

19   (XPS) (Fig. S5). The morphology, while minimally affected during early degradation times,

20   becomes riddled with micron sized features during later times (Fig. 1d), and the changes become

21   most obvious on similar timescales as those for which Pb^0 begins to appear in the XRD pattern.

22   The absorbance measurements appear to be the most sensitive for identifying this decomposition

23   mode (Fig. 1a), as indicated by the increase in sub-bandgap absorbance within the first 30 minutes

1   (inset of Fig. 1a). The only plausible species that could absorb sub-bandgap photons is a reduced

2   lead species. XRD and XPS provides insight that Pb^0 is present at advanced stages of degradation,

3   but we cannot preclude the presence of other reduced lead species, especially at earlier degradation

4   times.[20] After 120 minutes of exposure, the excess absorbance spectrum (spanning regions both

5   above and below the perovskite bandgap) closely resembles that of a ~5 nm film of elemental Pb^0

6   (see Fig. S6 for the absorption spectrum of Pb^0 thin films). In summary, the optoelectronic

7   properties of the perovskite film degrade significantly as defects associated with reduced lead

8   species are generated during LID. Notably, substantial losses in PL intensity occur well before any

9   significant changes in morphology or crystal structure are detectable, highlighting the importance

10   of optical measurements as essential early indicators of this degradation pathway. The QFLS

11   calculated from the PL quantum yield decays almost linearly, and while a solar cell using the films

12   under study as absorbers would limit degradation by trapping decomposition products and

13   extracting reactive charge carriers, reduced lead species formed during LID would deteriorate

14   photovoltaic performance via increased trap assisted recombination (resulting in V_{oc} decline) and

15   parasitic absorption (resulting in J_{sc} decline).[21]
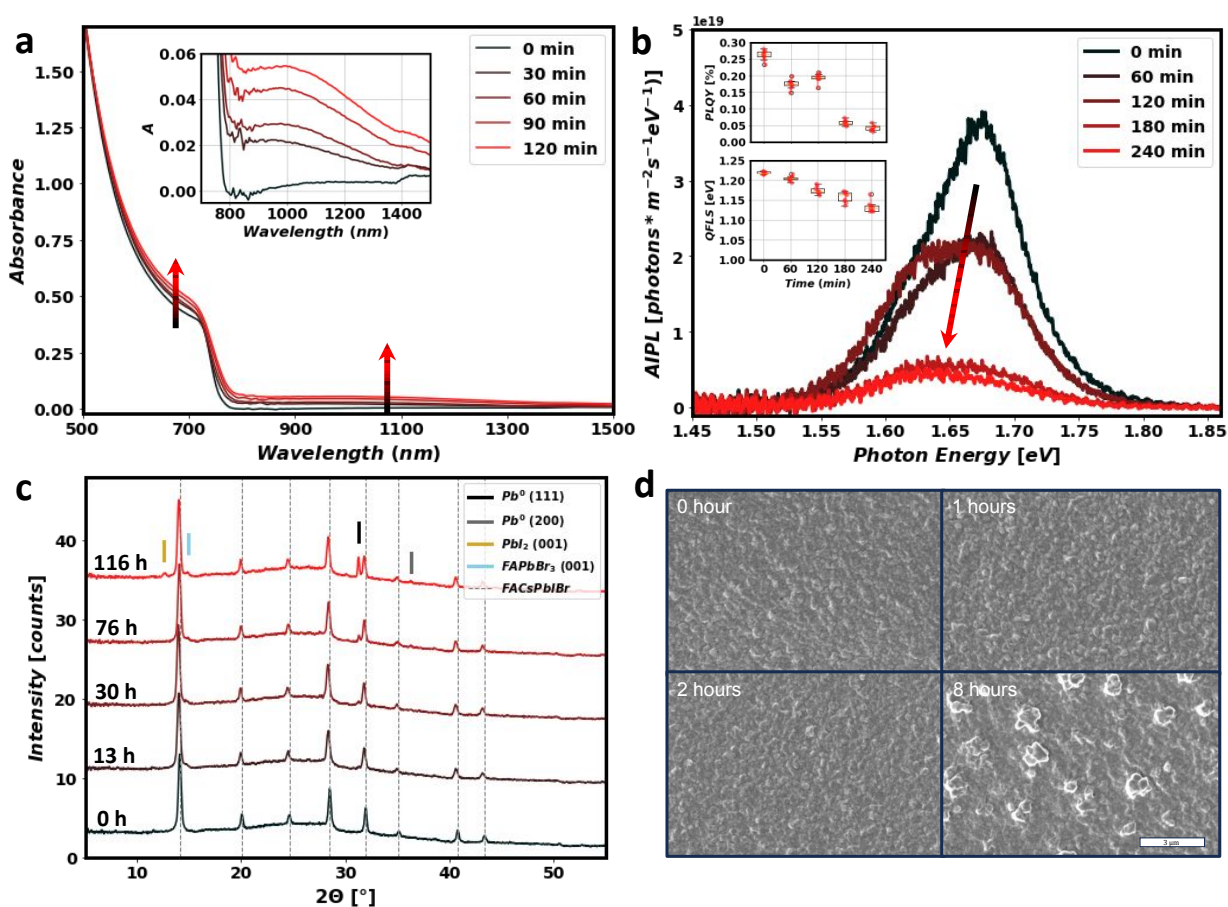
1
2 **Figure 1.** *Ex-situ* **characterization during degradation under 1 sun photon flux from a broad-**

3 **spectrum LED at 65°C in a dry N$_2$ atmosphere.** The changes in (a) absorbance, (b) AIPL

4 spectrum ($\lambda_{excitation} = 532\ nm$; 1 sun equivalent photon flux), (c) XRD pattern, and (d)

5 morphology (SEM images). Inset in panel (a) is a magnified view of the sub-bandgap region. Insets

6 in panel (b) are the *PLQY* and QFLS determined from the Ross relation (refer to SI section 1 for

7 these calculations). Special care is taken to ensure that samples are outside of a controlled N$_2$

8 environment for as little time as possible (typical ambient lab conditions are ~40% relative

9 humidity, 20°C; exposure during measurements is <30 minutes for XRD, <10 minutes for UV-

10 Vis-NIR, <10 minutes for SEM, and 0 minutes for AIPL). SEM measurements are taken on

11 separate samples to avoid conflating morphological effects of prolonged periods of vacuum

12 exposure with LID.

1   *Mechanism of Light-Induced Degradation*. The first reports of LID were of MAPbI$_3$ under

2   vacuum.[22,23] However, FA-rich compositions are also susceptible to LID[24] with several reports

3   observing hole trapping at grain boundaries which results in halide gas loss (X$_2$) and Pb^{2+} reduction

4   to Pb^0.[25–27] Material quality plays an important role in both initial optoelectronic device

5   performance and stability.[28,29] Defect-dense and/or heterogenous films have reduced barriers for

6   atomic, ionic, and molecular transport which increases the rate of material decomposition and

7   device performance degradation.[30–32] While many of these prior reports suggest that Pb^{2+} in the

8   perovskite lattice is directly reduced to Pb^0 during LID, other reports argue that the photolysis of

9   intermediate PbI$_2$ is the pathway to form Pb^0 (some noting that it is possible[33]).[20,21,34]

10   Kerner et al.[35] hypothesized that halide oxidation (h$^+$ + X$^-$ $\leftrightharpoons$ X$^{\cdot}$ $\leftrightharpoons$ $\frac{1}{2}$X$_2$) by valence band holes

11   (photoexcited or injected) can substantially increase halide species mobility (neutral X$^{\cdot}$ and X$_2$ are

12   assumed to be much more mobile than perovskite bound X$^-$) which can yield two related but

13   distinct phenomena. (1) If the halides settle in different domains, phase segregation results. The

14   perovskite lattice remains intact, but different domains of varying halide concentration exist.

15   Evidence of this behavior is typically observed with photoluminescence and electroluminescence

16   spectroscopy[36–38], and it is usually reversible after the incident light is removed.[19] (2) If halides

17   escape the perovskite lattice in the form of diatomic halide gases (X$_2$), decomposition occurs as

18   the perovskite is irreversibly converted to other chemical species.[39,40] It is worth noting that the

19   thermodynamics of halide vacancies[41] and the kinetics of species diffusion[42,43] are temperature

20   dependent with the latter following Arrhenius behavior. These prior reports provide insights into

21   the chemical processes that may be used to propose specific reaction pathways that in turn can be

22   used to derive rate expressions for this decomposition mode. Given that many other studies report

1   the formation of Pb^0 during LID, we operate under the assumption that the majority of the light-

2   induced defects are Pb^0, accounting for most of the near-infrared light absorption.

3   *Influence of Oxygen on LID*. Before proceeding with further investigations into the LID of

4   FACsPbIBr films, we seek to address how oxygen presence influences the degradation pathway.

5   While O_2 and H_2O vapor may be kept out of a PSC during fabrication and for some time with

6   encapsulation, even rigorous glass-glass encapsulation strategies with polyisobutylene (PIB) edge

7   seals cannot fully prevent diffusion of gaseous small molecules.[44,45] It is thus important to

8   understand how degradation will proceed if an environmental reactant diffuses through packaging

9   to meet the perovskite layer. To do so, we analyzed the change in optical absorbance when films

10   were subjected to various concentrations of ambient O_2 (0%, 3%, 10.5%, and 21%). In these

11   experiments, we placed FACsPbIBr films in environmental control chambers and illuminated them

12   with a broad-spectrum white LED (Fig. S3a). We measured the surface temperature with a contact

13   thermocouple and found it to be stable at 35°C. The flow rate of inlet gases is 3 L/min with the

14   desired oxygen concentration being achieved by mixing dry air and dry N_2.
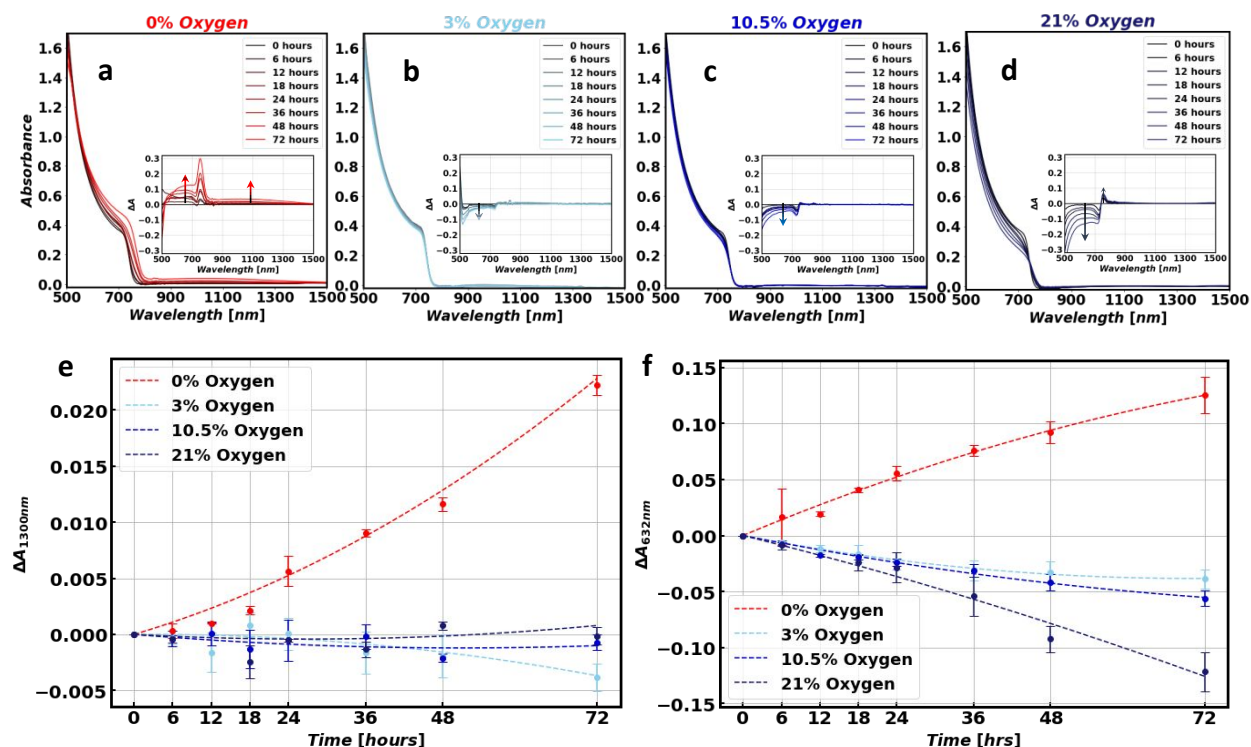
Figure 2. *Ex-situ* UV-Vis-NIR measurements during degradation at 35°C under 1 sun

equivalent illumination. Film absorbance over the course of degradation in dry atmospheres of

(a) 0%, (b) 3%, (c) 10.5%, and (d) 21% oxygen. Insets in a-d are the change in absorbance from

the initial time point with narrower vertical axes to emphasize the spectral changes over time. The

timeseries absorbance values at (e) 1300 nm and (f) 632 nm. Parabolic fits to the timeseries data

are included as dashed lines in (e) and (f) to guide the eye. Uncertainty is quantified by the standard

deviation (σ) of film absorbance change for 3 samples.

The results of these experiments are shown in Figure 2, demonstrating that 3% O_2 in the ambient

atmosphere is sufficient to prevent the accumulation of defects with near-infrared absorptivity

(Pb^0). Although none of the samples degraded in oxygen-containing environments accumulated

detectable levels of Pb^0, we infer that photooxidation processes did take place as evidenced by

decreases in above bandgap absorbance, with higher oxygen concentrations yielding higher rates

of decomposition. We speculate on the reason for O_2 preventing Pb^0 formation in SI section 8 and

1   hypothesize that it scavenges photogenerated electrons that would otherwise reduce Pb^{2+}.

2   Interestingly, examining Figure 2a and 2b reveals that the net effect of adding small amounts of

3   oxygen to an otherwise inert atmosphere is a slower rate of film decomposition. The inset in Figure

4   2a reveals an outsized increase in absorption as LID proceeds in the 700-800 nm region. This

5   behavior is observed to a lesser degree for degradation in 21% oxygen (inset of Fig. 2d). We

6   attribute this to an increase in disorder of the semiconductor (either static or dynamic) resulting in

7   increases in sub bandgap absorption in the region just below the bandgap (within ~0.1 eV).[46,47] As

8   such, we do not observe measurable absorption increases in this region for the films degraded in

9   3% or 10.5% oxygen atmospheres because they degrade less significantly (and thus induce less

10   additional disorder) than the films in 0% or 21% oxygen atmospheres. Importantly, the excess

11   absorption beyond ~800 nm shown in the inset of Figure 2a agrees with the Pb^0 absorption

12   spectrum shown in Figure S6, indicating that absorption measurements in the region >800 nm are

13   accurate for quantitative measurements of Pb^0 formation.

14
15   While film absorbance measurements provide valuable information about absorbing species

16   present in the film, the exact effect of any given degradation pathway on device relevant

17   optoelectronic properties is unknown from absorption measurements alone. To address this

18   missing link, we conducted *in-situ* measurements of film ambipolar diffusion length (L_D) and

19   photoluminescence quantum yield (*PLQY*) over the course of degradation in the same conditions

20   as the *ex-situ* experiments shown in Figure 2. To perform these measurements, we use a calibrated

21   widefield microscope for *PLQY* measurements and deposit gold contact pads on the FACsPbIBr

22   films with a thin channel (0.01 cm) for simultaneous two-point photoconductivity measurements

23   (Fig. 3a,b). From photoconductivity measurements, we can obtain an estimate for the L_D based on

24   sample geometry and photogeneration rate, which we have detailed in prior reports.[48,49] The results

1   of these experiments are shown in Figure 3. Diffusion length is a good proxy for how we expect

2   the film degradation to affect device performance as it unites both carrier transport and carrier

3   lifetime. The *PLQY* serves as a proxy for carrier lifetime alone, which helps disentangle changes

4   in diffusion length due to lifetime from those caused by changes in carrier mobility.

5   Degradation in pure N_2 results in monotonic decreases in both L_D and *PLQY*. The evolution of

6   the L_D is strongly correlated with that of the *PLQY*, suggesting that it may be almost entirely

7   explained by Pb^0 trap state formation. In contrast, the films placed in oxygen containing

8   atmospheres see an initial period of passivation (increasing L_D due to increasing minority carrier

9   lifetime) followed by degradation (decreasing L_D attributable to reduction in effective mobility

10   that likely arise from the buildup of insulating phases at grain boundaries). The kinetics of this

11   behavior accelerate as the environmental oxygen content increases, consistent with a

12   photooxidation mechanism that generates insulating byproducts that impede carrier transport.[48,50]

13   Note that the *PLQY* generally rises for each of the oxygen containing runs, indicating that the local

14   minority carrier lifetime is constant or increasing and suggesting that defect formation is not a

15   critical issue in these cases. While these photooxidation phenomena are not unique to these

16   perovskite compositions and have been reported previously for $MAPbI_3$,[42] the stark differences in

17   optoelectronic decay from relatively small differences in ambient atmosphere contents for this

18   perovskite composition is important because it indicates that relatively small amounts of oxygen

19   are sufficient to shift the dominant mode of decomposition. Again, this may signify a role of

20   oxygen as a particularly efficient scavenger of photogenerated electrons.[51] From the data shown

21   in Figures 2 and 3, we infer that there is likely an oxygen concentration between 0% and 3% at

22   which both mechanisms occur simultaneously but that concentrations $\geq 3\%$ appear to prevent

23   Pb^0 formation and are within the regime of purely photooxidation decomposition (all Pb^{2+} remains

1   oxidized). However, it is important to note that even for low-oxygen environments in which LID

2   is suppressed, apparent mobility losses can still quickly reduce the perovskite's optoelectronic

3   quality, highlighting the importance of retarding photooxidation as well as LID.

4   To assess and compare the relevant time scales of diffusion length decay among the different

5   degradation conditions, we define metrics of TL_D-80 and TL_D-90 which are defined as the time it

6   takes for the diffusion length to decrease to 80% and 90% of its original value, respectively. The

7   average TL_D-80 and TL_D-90 times ($\pm \sigma$) are displayed in table 1. Importantly, the films placed in

8   0% O_2 reach L_D-90 faster on average than the films placed in any of the oxygen containing

9   environments, highlighting the rapid optoelectronic performance decline that occurs during LID.
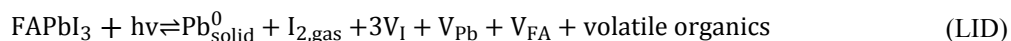
10

11
12
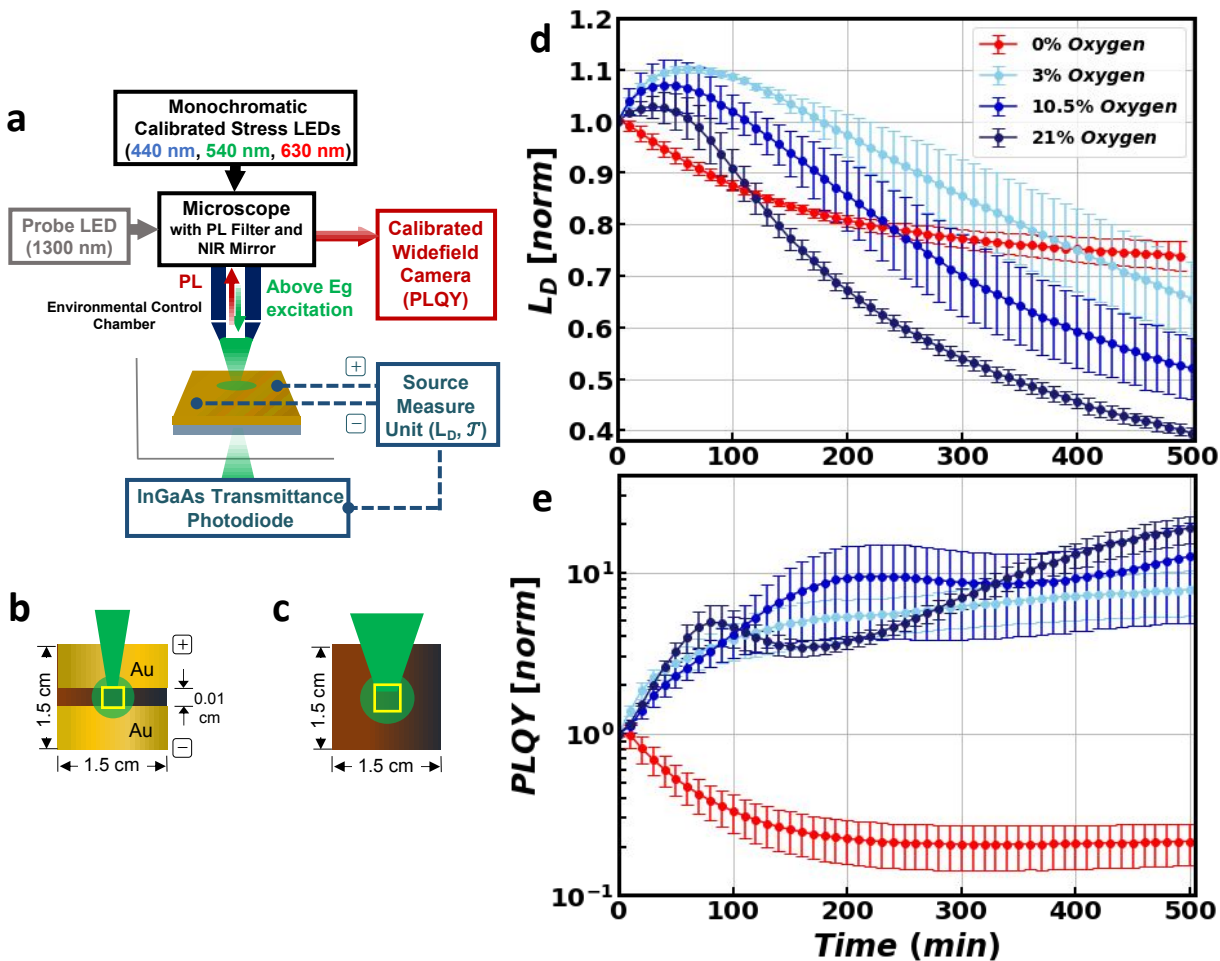
1   **Figure 3.** *In-situ* **optoelectronic performance trends for degradation in atmospheres of**

2   **varying oxygen concentration**. (a) Schematic of the *in-situ* microscope degradation experimental

3   apparatus which features a calibrated LED light source fed through an upright microscope and

4   shone through an objective lens onto the sample. Top-down view of perovskite samples with (b)

5   gold contacts (used for simultaneous collection of *PLQY* and L_D) and (c) bare (used for $\mathcal{T}_{1300\ nm}$

6   measurements). The normalized (d) ambipolar diffusion length and (e) photoluminescence

7   quantum yield under 10 sun equivalent photon flux at 65°C. Uncertainty is quantified by the

8   standard error of the mean ($\sigma/\sqrt{n}$) for 3 samples.

9   **Table 1.** TL_D**-80 and** TL_D**-90 Times for Degradation at 65°C, 1 sun under Different Ambient**

10   **Oxygen Concentrations**

[O$_2$]	TL$_D$-90 [min]	TL$_D$-80 [min]
0%	78 ± 20	293 ± 179
3%	285 ± 95	363 ± 115
10.5%	186 ± 74	242 ± 85
21%	97 ± 22	132 ± 20

11
12
13   *Measuring the Kinetics of Light-Induced Defect Formation*. Having established that light-

14   induced defect formation dominates the optoelectronic evolution of FACsPbIBr films in an inert

15   N$_2$ atmosphere under illumination, we proceed with the aim of measuring and predicting the

16   formation rate of these defects (with the assumption that most are Pb^0). We propose an overall net

17   reaction for this process that uses FAPbI$_3$ as an approximation of the mixed-cation, mixed-halide

18   composition. We do not expect the Cs or Br minorities to participate in important ways. To test

19   this assumption, we also test the photostability of FA$_{0.8}$Cs$_{0.2}$PbI$_3$ and FAPbI$_3$ thin films (Fig. S8).

1   We observe that the absorbance of both compositions increases in the sub bandgap region after a

2   period of photo-stress, indicating the universal susceptibility to LID of FA-rich compositions.

3   Notably, the rate of sub-bandgap absorption increase is slower for these compositions compared

4   to mixed-halide FACsPbIBr which agrees with the finding that halide alloying with bromine yields

5   less photostable materials.[52] Thus, the net total LID reaction can be written as the following:

6    $$FAPbI_3 + h\nu \rightleftharpoons Pb^0_{solid} + I_{2,gas} + 3V_I + V_{Pb} + V_{FA} + volatile\ organics \qquad \text{(LID)}$$

7   Section 5 of the SI discusses a plausible complete reaction mechanism with elementary steps for

8   the LID reaction. We arrive at a functional form for a mathematical expression to describe the

9   initial rate of Pb^0 formation (r_{Pb^0}) as a function of temperature and photon flux. Note that this

10   equation also happens to be identical to an empirical expression that could be written for the total

11   LID reaction.

12   $$r_{Pb^0} = k_{0,LID} exp\left(-\frac{E^{eff}_{A,LID}}{k_B T}\right) I^n_{in} \qquad (1)$$

13   Here, $k_{0,LID}$ is a temperature independent prefactor, $E^{eff}_{A,LID}$ is the effective activation energy, I_{in}

14   is the incident above bandgap photon flux, and n is the effective order of illumination.

15   We next proceed to measure the kinetics of the LID reaction to determine the various unknown

16   parameters contained within equation 1 for FACsPbIBr. We use a similar technique as in our

17   previous kinetic studies[17,18] on initial perovskite decomposition rate to determine the rate of Pb^0

18   formation (r_{Pb^0}). Information regarding the initial perovskite reaction rate has been shown to be

19   highly relevant for understanding and predicting device stability.[48,53] In short, we measure the

20   sample transmittance ($\mathcal{T}$) at 1300 nm (where reflectance changes minimally over the early times

21   of degradation, Fig. S7) in an *in-situ* degradation chamber (Fig. 3a,c) to obtain an estimate for

22   initial rate of absorbance change $\left(\frac{dA}{dt}\right)$. This allows us to quantify r_{Pb^0} by the following:

$$r_{Pb^0} = \frac{\rho_{Pb^0} \cdot log_{\mathrm{e}}(10)}{M_{Pb^0} \cdot \alpha_{1300\mathrm{nm}}} \cdot \frac{dA}{dt}$$

where ρ_{Pb^0} is the density, M_{Pb^0} is the molecular weight, and $\alpha_{1300\mathrm{nm}}$ is the absorption coefficient

at 1300 nm for Pb^0. Refer to SI section 4 for a detailed discussion of this derivation.
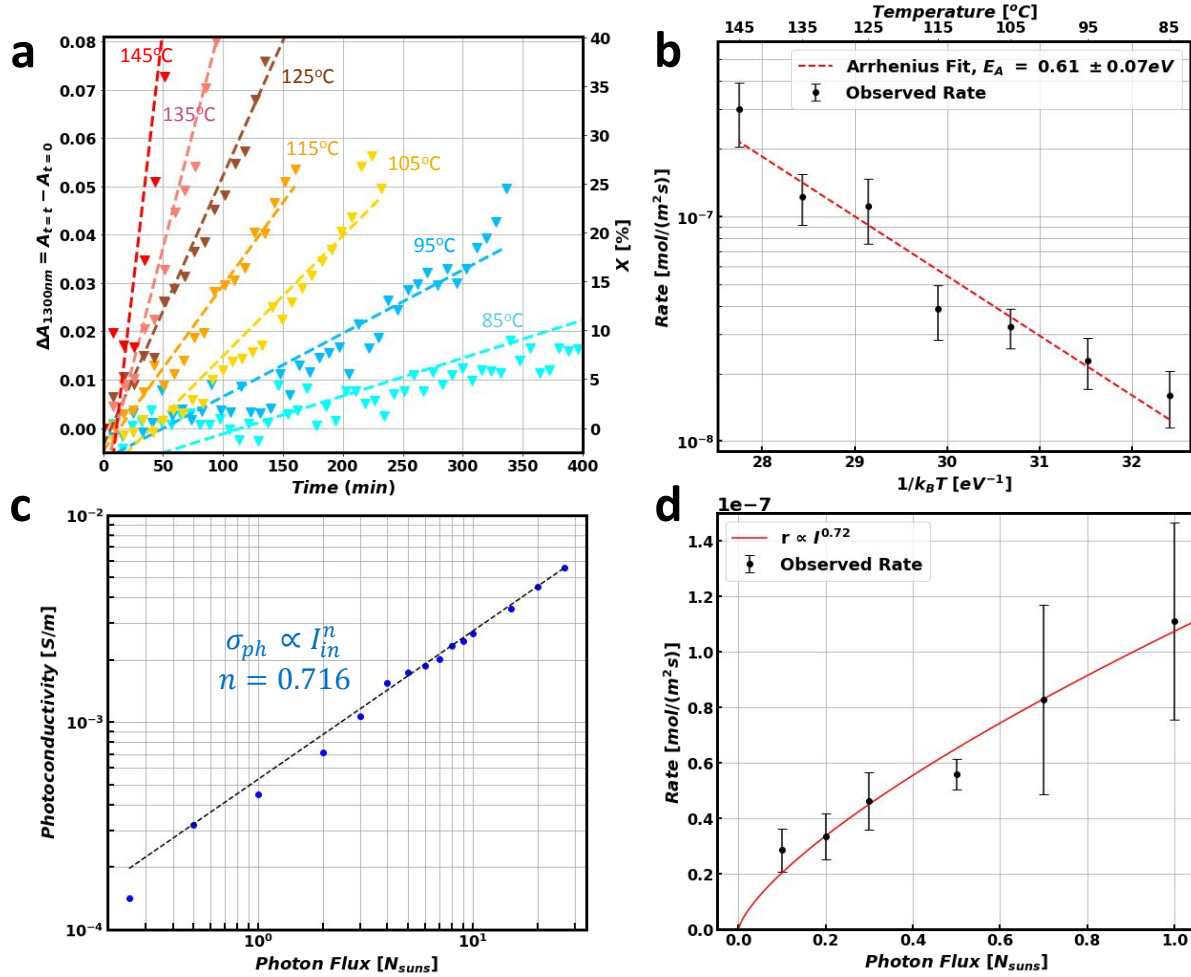
Figure 4. Determining model parameters. (a) Change in absorbance over time (with linear fits

to the data used to determine $\frac{dA}{dt}$) during degradation with 1 sun photon flux. Percent film

conversion to Pb^0 (X) is displayed on the right vertical axis. (b) Arrhenius plot for degradation

experiments under 1 sun illumination at varying temperatures. (c) Photoconductivity versus photon

flux with sublinear fit. (d) Initial Pb^0 formation rate as a function of incident photon flux at 125°C

with fit (exponent fixed to 0.72).

1　**Table 2. Best-Fit Parameters for the Light-Induced Pb^0 Formation Kinetic Model**

Parameter	Value	Unit
$E_{A,\,LID}^{eff}$	0.61 ± 0.07	eV
$k_{0,LID}$	$(3.55 \pm 0.58) \cdot 10^{-15}$	mol $\cdot$m$^{-2}\cdot$s$^{-1}\cdot$(photons$\cdot$m$^{-2}\cdot$s^{-1})$^{-0.72}$
n	0.72	unitless

2

3　　To determine parameters that define equation 1 ($E_{A,LID}^{eff}$, n, $k_{0,LID}$), we used monochromatic 540

4　nm illumination over a range of temperature and illumination conditions. We choose to measure

5　the rate of degradation at elevated temperatures (85 -145ºC) due to the relatively slow rate of this

6　reaction. We observe an Arrhenius relationship with respect to the effect of temperature on r_{Pb^0}

7　which suggests that this reaction is thermally activated. Thus, we expect the experimentally

8　determined parameters at elevated temperatures to remain accurate across a wide range of

9　temperature and illumination conditions. We demonstrate that decomposition due to elevated

10　temperature exposure, resulting in apparent loss of formamidinium, is negligible in comparison to

11　LID in SI section 9 (particularly with regards to its effects on film optical properties).

12　　Figure 4a displays typical data for the change in 1300 nm absorbance over time with linear fits

13　to that data. Degradation experiments from 85-145ºC under 1 sun equivalent photon flux are used

14　to determine the activation energy as ~0.61 eV (Fig. 4b). To determine the effective order of above

15　bandgap photons (n), we performed photoconductivity measurements as a function of incident

16　photon flux (Fig. 4c). We have shown previously that the activity of a photoexcited species is

17　directly proportional to the incident above bandgap photon flux raised to a constant value.[17]

18　Additional information on the relationship between photoconductivity and photoexcited species

19　activity is included in SI section 6. Here, we determine this value to be ~0.72 when measuring

20　across a range of photon fluxes (0.25 to ~29 suns). To confirm that this exponent accurately

1   captures the change in hole activity (posited to be the relevant photoexcited species) during light-

2   induced degradation, we measure r_{Pb^0} as a function of photon flux from 0.1-1 suns at 125°C (Fig.

3   4d). A fit of the data is excellent (refer to SI section 7 for further fitting details), indicating that we

4   have accurately captured the incremental activity of holes for increases in photon flux with our

5   power law model.

6   To determine $k_{0,LID}$, we take all degradation runs used to determine $E_{A,LID}^{eff}$ (1 sun, 85-145°C,

7   540 nm) and all runs used to confirm n (125°C, 0.1-1 sun, 540 nm) and perform a minimization

8   on the sum of the squared errors, which gives a result of $3.55 \times 10^{-15} \frac{mol}{m^2 s (photons \cdot m^2 s)^{0.72}}$. The

9   dataset used for this fitting is referred to as the 'training dataset' (42 samples). The best-fit

10   parameters for the kinetic rate model for Pb^0 formation are displayed in Table 2. Note that the

11   uncertainty estimates for $E_{A,LID}^{eff}$ and $k_{0,LID}$ are quantified by the standard error of the linear fits to

12   the Arrhenius plot and to the complete training dataset, respectively.

13   As mentioned previously, the debate around PbI_2 photolysis remains unanswered in the

14   perovskite community. First, we note that significant Pb^0 is formed during irradiation with 540 nm

15   light (E_{photon}=2.30 eV) which itself cannot excite PbI_2 by a band-band transition since it has an

16   energy below the bandgap of PbI_2 ($E_g \sim 2.35$ eV). Thus, while PbI_2 photolysis may occur in

17   perovskite samples with excess PbI_2 impurities, we note that this is not necessary to induce Pb^0

18   formation in our films and is not the mechanism that we observe since Pb^0 is formed even when

19   the incident beam has photon energies less than the bandgap of PbI_2. To confirm this finding, we

20   collected a new dataset (referred to as the 'test dataset' (28 samples)) that incorporates alternate

21   temperatures and illumination conditions for 540 nm illumination as well as 440 nm (well above

22   PbI_2 bandgap) and 630 nm illumination (well below PbI_2 bandgap). SI section 7 provides further

1   explanation of the conditions for the testing and training datasets and an expanded discussion of

2   the fitting procedure for the parameters of equation 1.

3   Figure 5a shows the results for the training dataset with median and mean error of 34% and 71%,

4   respectively. Figure 5b shows the results for the test dataset with median and mean error of 41%

5   and 41%, respectively. Despite some sample-to-sample variation, we see that the model

6   determined from the training dataset, which only considers a relatively small sliver of the

7   parameter space, can accurately predict r_{Pb^0} for varying temperatures, photon fluxes, and photon

8   energies. We emphasize that illumination wavelength within the visible regime minimally

9   influences the degradation rate. Figure 5c shows the degradation data for the 630 nm and 440 nm

10   illumination. This plot further emphasizes the goodness of the model fit and suggests that, if

11   anything, the lower energy 630 nm light produces higher degradation rates than 440 nm. These

12   results highlight that PbI_2 photolysis is not the mode of degradation that we observe en route to

13   Pb^0 formation and suggest that degradation mitigation strategies outside that of the PbI_2 photolysis

14   suppression framework must be considered to enhance perovskite longevity.
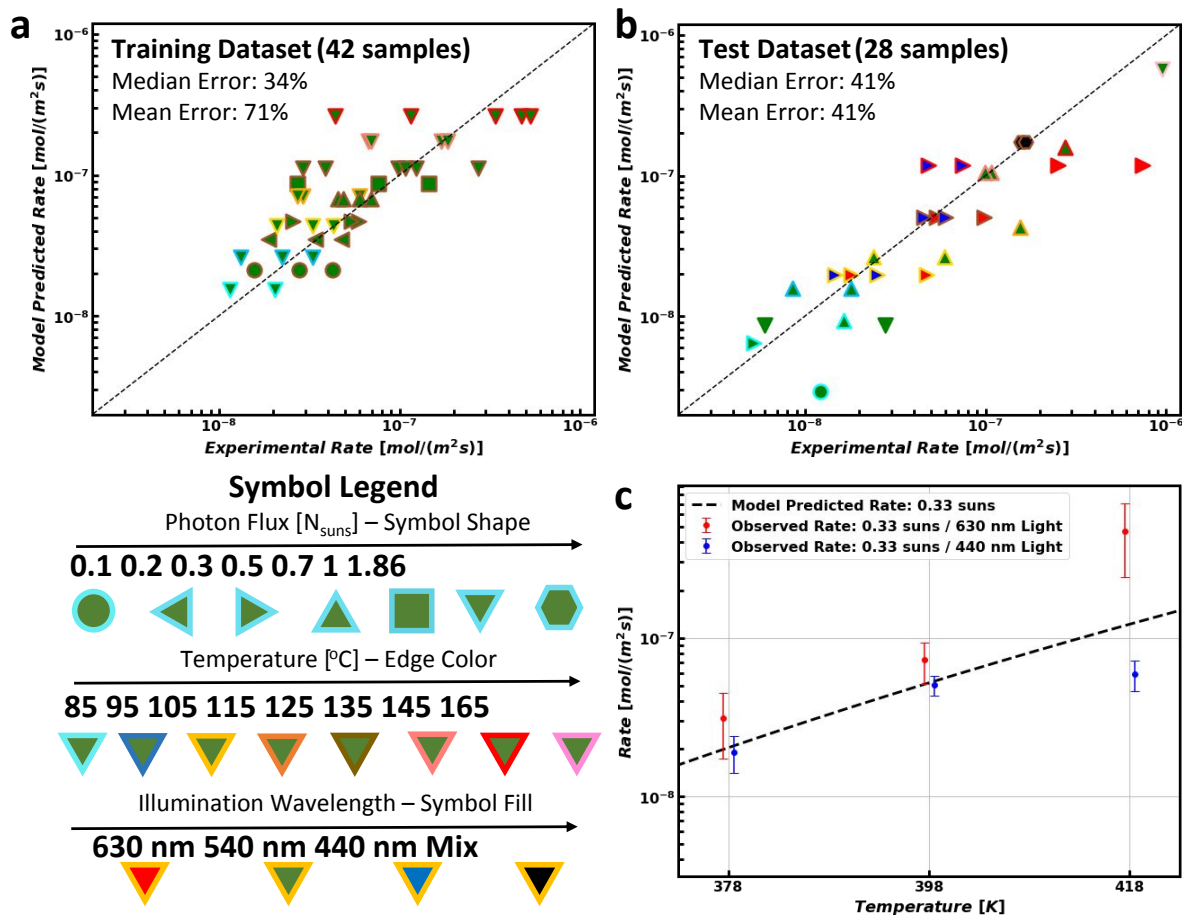
Figure 5. Light-induced Pb^0 formation rate model performance. (a) Parity plot for the training dataset and (b) for the test dataset. (c) Comparison of 630 nm monochromatic illumination (red) and 440 nm monochromatic illumination (blue) on Pb^0 rate. 630 nm and 440 nm photon fluxes are both set equal to 0.33 suns (5 x 10^{20} photons/m^2/s). Datapoints are sightly offset along the temperature axis for clarity.

Mitigation strategies for suppressing halide segregation and LID center around reducing halide mobility and escaping tendency from the perovskite. Device stacks with strong encapsulation will certainly slow volatile halide species loss and thus promote reverse decomposition reactions (e.g. Pb^0 + I$_2 \rightleftharpoons$ Pb^{2+} + 2I$^-$), slowing LID processes. We demonstrate that encapsulation slows Pb^0 formation in SI section 10. However, the intrinsic material instability related to mobile and reactive

1   ions will remain and prevent the realization of multidecade module service lifetimes if a promising

2   solution cannot be found. Promising paths towards reducing halide movement are via passivation

3   (which will necessarily slow diffusion due to fewer vacancies present in the lattice[54,55]) and by tin

4   substitution for lead (which shifts the valence band maximum above the halide defect energies and

5   slows halide oxidation[56,57]). Ultimately, mobile halides that facilitate decomposition present a

6   significant challenge for lead-based perovskite photovoltaic commercialization. We also would

7   like to emphasize that the trapping of volatile I_2 vapor can promote other decomposition pathways

8   (not just the reverse LID reaction) in a complete device stack.[58,59] As such, a complete picture of

9   PSC device degradation under inert conditions would include LID, its reverse reaction, and I_2

10 related oxidation reactions with the perovskite itself and other layers in the device stack.

11 In summary, we report, for the first-time, quantitative measurements of light-induced

12 degradation in a halide perovskite semiconductor. The degradation products of LID are reduced

13 lead species with broadband optical absorption and are very likely fully reduced Pb^0. We have

14 studied the effects of oxygen on this decomposition pathway and have derived a rate law for the

15 initial rate of Pb^0 formation and fit it to our quantitative measurements. We also show that the

16 wavelength distribution of the incident above bandgap photons negligibly influences the formation

17 rate. This work raises important questions regarding how to address oxygen ingress through

18 advanced encapsulation techniques, as well as how to manage the iodine species generated during

19 LID, both of which remain significant challenges for enhancing the stability of perovskite-based

20 devices.

21

22

23

1 **Supporting Information**

2 Detailed experimental methods, characterization of perovskite films and devices, data on light

3 sources used for degradation experiments, degradation product identification with XRD and XPS,

4 further information on the estimation of initial Pb^0 formation rate calculated from sub bandgap

5 transmittance and absorption coefficient of Pb^0, derivations of a rate expression for light-induced

6 degradation and for variation of photoactive species activity with photon flux, details of rate model

7 fitting and testing, discussion of the role of oxygen in preventing metallic lead formation,

8 comparison of degradation at high temperatures under illumination and in the dark, effects of

9 encapsulation on the rate of Pb^0 formation.

10 **AUTHOR INFORMATION**

11 **Corresponding Author**

12 Hugh W. Hillhouse - Department of Chemical Engineering, Clean Energy Institute, University of

13 Washington, Seattle, Washington 98195-1750, United States; http://orcid.org/0000-0003-2069-

14 7899; Email: h2@uw.edu

15 **Authors**

16 Spencer G. Cira - Department of Chemical Engineering, Clean Energy Institute, University of

17 Washington, Seattle, Washington 98195-1750, United States; https://orcid.org/0009-0003-5343-

18 7265

19 Wiley A. Dunlap-Shohl - Department of Chemical Engineering, Clean Energy Institute, University

20 of Washington, Seattle, Washington 98195-1750, United States; https://orcid.org/0000-0002-

21 3183-699X

1

2   Yuhuan Meng - Department of Chemical Engineering, Clean Energy Institute, University of

3   Washington, Seattle, Washington 98195-1750, United States; http://orcid.org/0000-0001-5821-

4   2872

5   Preetham P. Sunkari - Department of Chemical Engineering, Clean Energy Institute, University of

6   Washington, Seattle, Washington 98195-1750, United States

7   Jordi H. Folch - Department of Chemical Engineering, Clean Energy Institute, University of

8   Washington, Seattle, Washington 98195-1750, United States

9   **Conflicts of Interest**

10 There are no conflicts of interest to declare.

11 **Data Availability**

12 Data for this article are available at
13 https://osf.io/n7u2t/?view_only=4a251b2ae5f94aa0adb408efc7b0d4ca.
14
15 **Acknowledgements**

8

9

10

11

12
13
14
15
16
17
18
19
20
21
22
23
24
25
26
27
28
29
30
31
32
33
34
35

1   **References**

2   (1)   Vaynzof, Y. The Future of Perovskite Photovoltaics—Thermal Evaporation or Solution
3   Processing? *Adv Energy Mater* **2020**, *10* (48). https://doi.org/10.1002/aenm.202003073.
4   (2)   Stranks, S. D.; Eperon, G. E.; Grancini, G.; Menelaou, C.; Alcocer, M. J. P.; Leijtens, T.;
5   Herz, L. M.; Petrozza, A.; Snaith, H. J. Electron-Hole Diffusion Lengths Exceeding 1
6   Micrometer in an Organometal Trihalide Perovskite Absorber. *Science (1979)* **2013**, *342*.
7   (3)   Kojima, A.; Teshima, K.; Shirai, Y.; Miyasaka, T. Organometal Halide Perovskites as
8   Visible-Light Sensitizers for Photovoltaic Cells. *J Am Chem Soc* **2009**, *131* (17), 6050–
9   6051. https://doi.org/10.1021/ja809598r.
10   (4)   Tao, S.; Schmidt, I.; Brocks, G.; Jiang, J.; Tranca, I.; Meerholz, K.; Olthof, S. Absolute
11   Energy Level Positions in Tin- and Lead-Based Halide Perovskites. *Nat Commun* **2019**,
12   *10* (1). https://doi.org/10.1038/s41467-019-10468-7.
13   (5)   NREL Best Research-Cell Efficiency Data Table. Accessed December 10, 2024.
14   (6)   Ni, Z.; Bao, C.; Liu, Y.; Jiang, Q.; Wu, W.-Q.; Chen, S.; Dai, X.; Chen, B.; Hartweg, B.;
15   Yu, Z.; Holman, Z.; Huang, J. *Resolving Spatial and Energetic Distributions of Trap
16   States in Metal Halide Perovskite Solar Cells*. https://www.science.org.
17   (7)   Futscher, M. H.; Gangishetty, M. K.; Congreve, D. N.; Ehrler, B. Quantifying Mobile Ions
18   and Electronic Defects in Perovskite-Based Devices with Temperature-Dependent
19   Capacitance Measurements: Frequency vs Time Domain. *Journal of Chemical Physics*
20   **2020**, *152* (4). https://doi.org/10.1063/1.5132754.
21   (8)   Siekmann, J.; Ravishankar, S.; Kirchartz, T. Apparent Defect Densities in Halide
22   Perovskite Thin Films and Single Crystals. *ACS Energy Letters*. American Chemical
23   Society September 10, 2021, pp 3244–3251.
24   https://doi.org/10.1021/acsenergylett.1c01449.
25   (9)   Steirer, K. X.; Schulz, P.; Teeter, G.; Stevanovic, V.; Yang, M.; Zhu, K.; Berry, J. J.
26   Defect Tolerance in Methylammonium Lead Triiodide Perovskite. *ACS Energy Lett* **2016**,
27   *1* (2), 360–366. https://doi.org/10.1021/acsenergylett.6b00196.
28   (10)   Kim, G. W.; Petrozza, A. Defect Tolerance and Intolerance in Metal-Halide Perovskites.
29   *Advanced Energy Materials*. Wiley-VCH Verlag October 1, 2020.
30   https://doi.org/10.1002/aenm.202001959.
31   (11)   Boyd, C. C.; Cheacharoen, R.; Leijtens, T.; McGehee, M. D. Understanding Degradation
32   Mechanisms and Improving Stability of Perovskite Photovoltaics. *Chemical Reviews*.
33   American Chemical Society March 13, 2019, pp 3418–3451.
34   https://doi.org/10.1021/acs.chemrev.8b00336.
35   (12)   Xiao, Z.; Zhou, Y.; Hosono, H.; Kamiya, T.; Padture, N. P. Bandgap Optimization of
36   Perovskite Semiconductors for Photovoltaic Applications. *Chemistry - A European
37   Journal*. Wiley-VCH Verlag February 16, 2018, pp 2305–2316.
38   https://doi.org/10.1002/chem.201705031.
39   (13)   Berhe, T. A.; Su, W. N.; Chen, C. H.; Pan, C. J.; Cheng, J. H.; Chen, H. M.; Tsai, M. C.;
40   Chen, L. Y.; Dubale, A. A.; Hwang, B. J. Organometal Halide Perovskite Solar Cells:
41   Degradation and Stability. *Energy and Environmental Science*. Royal Society of
42   Chemistry February 1, 2016, pp 323–356. https://doi.org/10.1039/c5ee02733k.
43   (14)   Jeon, N. J.; Noh, J. H.; Yang, W. S.; Kim, Y. C.; Ryu, S.; Seo, J.; Seok, S. Il.
44   Compositional Engineering of Perovskite Materials for High-Performance Solar Cells.
45   *Nature* **2015**, *517* (7535), 476–480. https://doi.org/10.1038/nature14133.

1   (15) Dunfield, S. P.; Bliss, L.; Zhang, F.; Luther, J. M.; Zhu, K.; van Hest, M. F. A. M.; Reese,
2   M. O.; Berry, J. J. From Defects to Degradation: A Mechanistic Understanding of
3   Degradation in Perovskite Solar Cell Devices and Modules. *Advanced Energy Materials*.
4   Wiley-VCH Verlag July 1, 2020. https://doi.org/10.1002/aenm.201904054.

5   (16) Ma, S.; Yuan, G.; Zhang, Y.; Yang, N.; Li, Y.; Chen, Q. Development of Encapsulation
6   Strategies towards the Commercialization of Perovskite Solar Cells. *Energy and*
7   *Environmental Science*. Royal Society of Chemistry January 1, 2022, pp 13–55.
8   https://doi.org/10.1039/d1ee02882k.

9   (17) Siegler, T. D.; Dunlap-Shohl, W. A.; Meng, Y.; Yang, Y.; Kau, W. F.; Sunkari, P. P.;
10   Tsai, C. E.; Armstrong, Z. J.; Chen, Y. C.; Beck, D. A. C.; Meilă, M.; Hillhouse, H. W.
11   Water-Accelerated Photooxidation of CH3NH3PbI3Perovskite. *J Am Chem Soc* **2022**, *144*
12   (12), 5552–5561. https://doi.org/10.1021/jacs.2c00391.

13   (18) Meng, Y.; Sunkari, P. P.; Meilă, M.; Hillhouse, H. W. Chemical Reaction Kinetics of the
14   Decomposition of Low-Bandgap Tin-Lead Halide Perovskite Films and the Effect on the
15   Ambipolar Diffusion Length. *ACS Energy Lett* **2023**, *8* (4), 1688–1696.
16   https://doi.org/10.1021/acsenergylett.2c02733.

17   (19) Hoke, E. T.; Slotcavage, D. J.; Dohner, E. R.; Bowring, A. R.; Karunadasa, H. I.;
18   McGehee, M. D. Reversible Photo-Induced Trap Formation in Mixed-Halide Hybrid
19   Perovskites for Photovoltaics. *Chem Sci* **2015**, *6* (1), 613–617.
20   https://doi.org/10.1039/c4sc03141e.

21   (20) Lu, Y.; Hu, J.; Ge, Y.; Tian, B.; Zhang, Z.; Sui, M. Decisive Influence of Amorphous
22   PbI2−xon the Photodegradation of Halide Perovskites. *J Mater Chem A Mater* **2021**, *9*
23   (26), 15059–15067. https://doi.org/10.1039/d1ta01730f.

24   (21) Liang, J.; Hu, X.; Wang, C.; Liang, C.; Chen, C.; Xiao, M.; Li, J.; Tao, C.; Xing, G.; Yu,
25   R.; Ke, W.; Fang, G. Origins and Influences of Metallic Lead in Perovskite Solar Cells.
26   *Joule* **2022**, *6* (4), 816–833. https://doi.org/10.1016/j.joule.2022.03.005.

27   (22) Juarez-Perez, E. J.; Ono, L. K.; Maeda, M.; Jiang, Y.; Hawash, Z.; Qi, Y.
28   Photodecomposition and Thermal Decomposition in Methylammonium Halide Lead
29   Perovskites and Inferred Design Principles to Increase Photovoltaic Device Stability. *J*
30   *Mater Chem A Mater* **2018**, *6* (20), 9604–9612. https://doi.org/10.1039/c8ta03501f.

31   (23) Li, Y.; Xu, X.; Wang, C.; Ecker, B.; Yang, J.; Huang, J.; Gao, Y. Light-Induced
32   Degradation of CH3NH3PbI3 Hybrid Perovskite Thin Film. *Journal of Physical*
33   *Chemistry C* **2017**, *121* (7), 3904–3910. https://doi.org/10.1021/acs.jpcc.6b11853.

34   (24) Kim, G. Y.; Senocrate, A.; Yang, T. Y.; Gregori, G.; Grätzel, M.; Maier, J. Large Tunable
35   Photoeffect on Ion Conduction in Halide Perovskites and Implications for
36   Photodecomposition. *Nat Mater* **2018**, *17* (5), 445–449. https://doi.org/10.1038/s41563-
37   018-0038-0.

38   (25) Doherty, T. A. S.; Winchester, A. J.; Macpherson, S.; Johnstone, D. N.; Pareek, V.;
39   Tennyson, E. M.; Kosar, S.; Kosasih, F. U.; Anaya, M.; Abdi-Jalebi, M.; Andaji-
40   Garmaroudi, Z.; Wong, E. L.; Madéo, J.; Chiang, Y. H.; Park, J. S.; Jung, Y. K.;
41   Petoukhoff, C. E.; Divitini, G.; Man, M. K. L.; Ducati, C.; Walsh, A.; Midgley, P. A.;
42   Dani, K. M.; Stranks, S. D. Performance-Limiting Nanoscale Trap Clusters at Grain
43   Junctions in Halide Perovskites. *Nature* **2020**, *580* (7803), 360–366.
44   https://doi.org/10.1038/s41586-020-2184-1.

45   (26) Macpherson, S.; Doherty, T. A. S.; Winchester, A. J.; Kosar, S.; Johnstone, D. N.; Chiang,
46   Y. H.; Galkowski, K.; Anaya, M.; Frohna, K.; Iqbal, A. N.; Nagane, S.; Roose, B.; Andaji-

Garmaroudi, Z.; Orr, K. W. P.; Parker, J. E.; Midgley, P. A.; Dani, K. M.; Stranks, S. D. Local Nanoscale Phase Impurities Are Degradation Sites in Halide Perovskites. *Nature* **2022**, *607* (7918), 294–300. https://doi.org/10.1038/s41586-022-04872-1.

(27)　Ducati, C.; Ferrer Orri, J.; Yang, T.; Doherty, T.; Selby, T.; Chiang, Y.-H.; Anaya, M.; Allen, C. Visualising Nanoscale Bias-Induced Degradation in Halide Perovskite Solar Absorbers. **2023**. https://doi.org/10.21203/rs.3.rs-3224875/v1.

(28)　Bai, Y.; Huang, Z.; Zhang, X.; Lu, J.; Niu, X.; He, Z.; Zhu, C.; Xiao, M.; Song, Q.; Wei, X.; Wang, C.; Cui, Z.; Dou, J.; Chen, Y.; Pei, F.; Zai, H.; Wang, W.; Song, T.; An, P.; Zhang, J.; Dong, J.; Li, Y.; Shi, J.; Jin, H.; Chen, P.; Sun, Y.; Li, Y.; Chen, H.; Wei, Z.; Zhou, H.; Chen, Q. *Initializing Film Homogeneity to Retard Phase Segregation for Stable Perovskite Solar Cells*. https://www.science.org.

(29)　Frohna, K.; Anaya, M.; Macpherson, S.; Sung, J.; Doherty, T. A. S.; Chiang, Y. H.; Winchester, A. J.; Orr, K. W. P.; Parker, J. E.; Quinn, P. D.; Dani, K. M.; Rao, A.; Stranks, S. D. Nanoscale Chemical Heterogeneity Dominates the Optoelectronic Response of Alloyed Perovskite Solar Cells. *Nat Nanotechnol* **2022**, *17* (2), 190–196. https://doi.org/10.1038/s41565-021-01019-7.

(30)　Wang, M.; Fei, C.; Uddin, A.; Huang, J. *Influence of Voids on the Thermal and Light Stability of Perovskite Solar Cells*; 2022; Vol. 8. https://www.science.org.

(31)　McGovern, L.; Grimaldi, G.; Futscher, M. H.; Hutter, E. M.; Muscarella, L. A.; Schmidt, M. C.; Ehrler, B. Reduced Barrier for Ion Migration in Mixed-Halide Perovskites. *ACS Appl Energy Mater* **2021**, *4* (12), 13431–13437. https://doi.org/10.1021/acsaem.1c03095.

(32)　Mundt, L. E.; Zhang, F.; Palmstrom, A. F.; Xu, J.; Tirawat, R.; Kelly, L. L.; Stone, K. H.; Zhu, K.; Berry, J. J.; Toney, M. F.; Schelhas, L. T. Mixing Matters: Nanoscale Heterogeneity and Stability in Metal Halide Perovskite Solar Cells. *ACS Energy Lett* **2022**, *7* (1), 471–480. https://doi.org/10.1021/acsenergylett.1c02338.

(33)　Roose, B.; Dey, K.; Chiang, Y. H.; Friend, R. H.; Stranks, S. D. Critical Assessment of the Use of Excess Lead Iodide in Lead Halide Perovskite Solar Cells. *Journal of Physical Chemistry Letters* **2020**, *11* (16), 6505–6512. https://doi.org/10.1021/acs.jpclett.0c01820.

(34)　Donakowski, A.; Miller, D. W.; Anderson, N. C.; Ruth, A.; Sanehira, E. M.; Berry, J. J.; Irwin, M. D.; Rockett, A.; Steirer, K. X. Improving Photostability of Cesium-Doped Formamidinium Lead Triiodide Perovskite. *ACS Energy Lett* **2021**, *6* (2), 574–580. https://doi.org/10.1021/acsenergylett.0c02339.

(35)　Kerner, R. A.; Xu, Z.; Larson, B. W.; Rand, B. P. The Role of Halide Oxidation in Perovskite Halide Phase Separation. *Joule*. Cell Press September 15, 2021, pp 2273–2295. https://doi.org/10.1016/j.joule.2021.07.011.

(36)　Hoke, E. T.; Slotcavage, D. J.; Dohner, E. R.; Bowring, A. R.; Karunadasa, H. I.; McGehee, M. D. Reversible Photo-Induced Trap Formation in Mixed-Halide Hybrid Perovskites for Photovoltaics. *Chem Sci* **2015**, *6* (1), 613–617. https://doi.org/10.1039/c4sc03141e.

(37)　Braly, I. L.; Stoddard, R. J.; Rajagopal, A.; Uhl, A. R.; Katahara, J. K.; Jen, A. K. Y.; Hillhouse, H. W. Current-Induced Phase Segregation in Mixed Halide Hybrid Perovskites and Its Impact on Two-Terminal Tandem Solar Cell Design. *ACS Energy Lett* **2017**, *2* (8), 1841–1847. https://doi.org/10.1021/acsenergylett.7b00525.

(38)　Dubose, J. T.; Kamat, P. V. Hole Trapping in Halide Perovskites Induces Phase Segregation. *Acc Mater Res* **2022**, *3* (7), 761–771. https://doi.org/10.1021/accountsmr.2c00076.

1   (39) Mathew, P. S.; Mathew, P. S.; Samu, G. F.; Samu, G. F.; Janáky, C.; Kamat, P. V.;
2   Kamat, P. V.; Kamat, P. V. Iodine (I) Expulsion at Photoirradiated Mixed Halide
3   Perovskite Interface. Should i Stay or Should i Go? *ACS Energy Lett* **2020**, *5* (6), 1872–
4   1880. https://doi.org/10.1021/acsenergylett.0c00925.
5   (40) Samu, G. F.; Balog, Á.; De Angelis, F.; Meggiolaro, D.; Kamat, P. V.; Janáky, C.
6   Electrochemical Hole Injection Selectively Expels Iodide from Mixed Halide Perovskite
7   Films. *J Am Chem Soc* **2019**, *141* (27), 10812–10820.
8   https://doi.org/10.1021/jacs.9b04568.
9   (41) Barboni, D.; De Souza, R. A. The Thermodynamics and Kinetics of Iodine Vacancies in
10   the Hybrid Perovskite Methylammonium Lead Iodide. *Energy Environ Sci* **2018**, *11* (11),
11   3266–3274. https://doi.org/10.1039/c8ee01697f.
12 (42) Elmelund, T.; Seger, B.; Kuno, M.; Kamat, P. V. How Interplay between Photo and
13   Thermal Activation Dictates Halide Ion Segregation in Mixed Halide Perovskites. *ACS*
14   *Energy Lett* **2020**, *5* (1), 56–63. https://doi.org/10.1021/acsenergylett.9b02265.
15 (43) Rosales, B. A.; Schutt, K.; Berry, J. J.; Wheeler, L. M. Leveraging Low-Energy Structural
16   Thermodynamics in Halide Perovskites. *ACS Energy Letters*. American Chemical Society
17   April 14, 2023, pp 1705–1715. https://doi.org/10.1021/acsenergylett.2c02698.
18 (44) Boyd, R. H.; Pant, P. V. K. *Molecular Packing and Diffusion in Polyisobutylene*; 1991;
19   Vol. 24. https://pubs.acs.org/sharingguidelines.
20 (45) Kempe, M. D.; Nobles, D. L.; Postak, L.; Calderon, J. A. Moisture Ingress Prediction in
21   Polyisobutylene-Based Edge Seal with Molecular Sieve Desiccant. *Progress in*
22   *Photovoltaics: Research and Applications* **2018**, *26* (2), 93–101.
23   https://doi.org/10.1002/pip.2947.
24 (46) Liu, Y.; Banon, J. P.; Frohna, K.; Chiang, Y. H.; Tumen-Ulzii, G.; Stranks, S. D.; Filoche,
25   M.; Friend, R. H. The Electronic Disorder Landscape of Mixed Halide Perovskites. *ACS*
26   *Energy Lett* **2023**, *8* (1), 250–258. https://doi.org/10.1021/acsenergylett.2c02352.
27 (47) Zeiske, S.; Sandberg, O. J.; Zarrabi, N.; Wolff, C. M.; Raoufi, M.; Peña-Camargo, F.;
28   Gutierrez-Partida, E.; Meredith, P.; Stolterfoht, M.; Armin, A. Static Disorder in Lead
29   Halide Perovskites. *Journal of Physical Chemistry Letters* **2022**, *13* (31), 7280–7285.
30   https://doi.org/10.1021/acs.jpclett.2c01652.
31 (48) Stoddard, R. J.; Dunlap-Shohl, W. A.; Qiao, H.; Meng, Y.; Kau, W. F.; Hillhouse, H. W.
32   Forecasting the Decay of Hybrid Perovskite Performance Using Optical Transmittance or
33   Reflected Dark-Field Imaging. *ACS Energy Lett* **2020**, *5* (3), 946–954.
34   https://doi.org/10.1021/acsenergylett.0c00164.
35 (49) Braly, I. L.; Stoddard, R. J.; Rajagopal, A.; Jen, A. K. Y.; Hillhouse, H. W.
36   Photoluminescence and Photoconductivity to Assess Maximum Open-Circuit Voltage and
37   Carrier Transport in Hybrid Perovskites and Other Photovoltaic Materials. *Journal of*
38   *Physical Chemistry Letters*. American Chemical Society July 5, 2018, pp 3779–3792.
39   https://doi.org/10.1021/acs.jpclett.8b01152.
40 (50) Aristidou, N.; Eames, C.; Sanchez-Molina, I.; Bu, X.; Kosco, J.; Saiful Islam, M.; Haque,
41   S. A. Fast Oxygen Diffusion and Iodide Defects Mediate Oxygen-Induced Degradation of
42   Perovskite Solar Cells. *Nat Commun* **2017**, *8*. https://doi.org/10.1038/ncomms15218.
43 (51) Aristidou, N.; Sanchez-Molina, I.; Chotchuangchutchaval, T.; Brown, M.; Martinez, L.;
44   Rath, T.; Haque, S. A. The Role of Oxygen in the Degradation of Methylammonium Lead
45   Trihalide Perovskite Photoactive Layers. *Angewandte Chemie* **2015**, *127* (28), 8326–8330.
46   https://doi.org/10.1002/ange.201503153.

1   (52)   Iqbal, A. N.; Orr, K. W. P.; Nagane, S.; Orri, J. F.; Doherty, T. A. S.; Jung, Y.; Chiang,
2   Y.; Selby, T. A.; Lu, Y.; Mirabelli, A. J.; Baldwin, A.; Ooi, Z. Y.; Gu, Q.; Anaya, M.;
3   Stranks, S. D. Composition Dictates Octahedral Tilt and Photostability in Halide
4   Perovskites. *Advanced Materials* **2024**. https://doi.org/10.1002/adma.202307508.
5   (53)   Dunlap-Shohl, W. A.; Meng, Y.; Sunkari, P. P.; Beck, D. A. C.; Meilă, M.; Hillhouse, H.
6   W. Physiochemical Machine Learning Models Predict Operational Lifetimes of $CH_3NH_3PbI_3$
7   Perovskite Solar Cells. *J Mater Chem A Mater* **2024**, *12* (16), 9730–9746.
8   https://doi.org/10.1039/D3TA06668A.
9   (54)   Taddei, M.; Smith, J. A.; Gallant, B. M.; Zhou, S.; Westbrook, R. J. E.; Shi, Y.; Wang, J.;
10   Drysdale, J. N.; McCarthy, D. P.; Barlow, S.; Marder, S. R.; Snaith, H. J.; Ginger, D. S.
11   Ethylenediamine Addition Improves Performance and Suppresses Phase Instabilities in
12   Mixed-Halide Perovskites. *ACS Energy Lett* **2022**, *7* (12), 4265–4273.
13   https://doi.org/10.1021/acsenergylett.2c01998.
14 (55)   Martani, S.; Zhou, Y.; Poli, I.; Aktas, E.; Meggiolaro, D.; Jiménez-López, J.; Wong, E. L.;
15   Gregori, L.; Prato, M.; Di Girolamo, D.; Abate, A.; De Angelis, F.; Petrozza, A. Defect
16   Engineering to Achieve Photostable Wide Bandgap Metal Halide Perovskites. *ACS*
17   *Energy Lett* **2023**, *8* (6), 2801–2808. https://doi.org/10.1021/acsenergylett.3c00610.
18 (56)   Senanayak, S. P.; Dey, K.; Shivanna, R.; Li, W.; Ghosh, D.; Zhang, Y.; Roose, B.;
19   Zelewski, S. J.; Andaji-Garmaroudi, Z.; Wood, W.; Tiwale, N.; MacManus-Driscoll, J. L.;
20   Friend, R. H.; Stranks, S. D.; Sirringhaus, H. Charge Transport in Mixed Metal Halide
21   Perovskite Semiconductors. *Nat Mater* **2023**, *22* (2), 216–224.
22   https://doi.org/10.1038/s41563-022-01448-2.
23 (57)   Dey, K.; Ghosh, D.; Pilot, M.; Pering, S. R.; Roose, B.; Deswal, P.; Senanayak, S. P.;
24   Cameron, P. J.; Islam, M. S.; Stranks, S. D. Substitution of Lead with Tin Suppresses
25   Ionic Transport in Halide Perovskite Optoelectronics. *Energy Environ Sci* **2023**, *17* (2),
26   760–769. https://doi.org/10.1039/d3ee03772j.
27 (58)   Fu, F.; Pisoni, S.; Jeangros, Q.; Sastre-Pellicer, J.; Kawecki, M.; Paracchino, A.; Moser,
28   T.; Werner, J.; Andres, C.; Duchêne, L.; Fiala, P.; Rawlence, M.; Nicolay, S.; Ballif, C.;
29   Tiwari, A. N.; Buecheler, S. I2 Vapor-Induced Degradation of Formamidinium Lead
30   Iodide Based Perovskite Solar Cells under Heat-Light Soaking Conditions. *Energy*
31   *Environ Sci* **2019**, *12* (10), 3074–3088. https://doi.org/10.1039/c9ee02043h.
32 (59)   Wang, S.; Jiang, Y.; Juarez-Perez, E. J.; Ono, L. K.; Qi, Y. Accelerated Degradation of
33   Methylammonium Lead Iodide Perovskites Induced by Exposure to Iodine Vapour. *Nat*
34   *Energy* **2017**, *2* (1). https://doi.org/10.1038/nenergy.2016.195.
35